Marine and Petroleum Geology 108 (2019) 368–376

Contents lists available at ScienceDirect

Marine and Petroleum Geology

journal homepage: www.elsevier.com/locate/marpetgeo

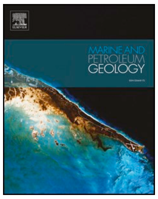

Research paper

Constraints on the fluid supply rate into and through gas hydrate reservoir systems as inferred from pore-water chloride and in situ temperature profiles, Krishna-Godavari Basin, India

Masataka Kinoshita[a,b,*], Akira Ijiri[c,d], Satoru Haraguchi[e], Francisco Jose Jiménez-Espejo[f], Nobuharu Komai[g], Hisami Suga[f], Takamitsu Sugihara[h], Wataru Tanikawa[c,d], Takehiro Hirose[b,c], Yohei Hamada[b,c], Lallan P. Gupta[c], Naokazu Ahagon[c], Yuka Masaki[d], Natsue Abe[b], Hung Y. Wu[b], Shun Nomura[i], Weiren Lin[j], Yuzuru Yamamoto[b], Yasuhiro Yamada[b], NGHP Expedition JAMSTEC Science Team

[a] *Earthquake Research Institute, The University of Tokyo, Japan*
[b] *R & D Center for Ocean Drilling Science, JAMSTEC, 3173-25 Showa-machi, Yokohama, 236-0001, Japan*
[c] *Kochi Institute for Core Sample Research, Japan Agency for Marine-Earth Science and Technology (JAMSTEC), 200 Monobe otsu, Nankoku, 783-8502, Japan*
[d] *R & D Center for Submarine Resources, JAMSTEC, Natsushima-cho 2-15, Yokosuka, 237-0061, Japan*
[e] *Department of Solid Earth Geochemistry, JAMSTEC, Natsushima-cho 2-15, Yokosuka, 237-0061, Japan*
[f] *Department of Biogeochemistry, JAMSTEC, Natsushima-cho 2-15, Yokosuka, 237-0061, Japan*
[g] *Marine Works Japan Ltd., 3-54-1 Oppamahigashi, Yokosuka, 237-0063, Japan*
[h] *CDEX, JAMSTEC, Japan*
[i] *Dept. Mathematical Science & Adv. Tech., JAMSTEC, 3173-25 Showa-machi, 29 Yokohama, 236-0001, Japan*
[j] *Earth & Resource System, Dept. Urban Management, Kyoto University, Katsura C, 31 Nishikyo, 615-8530, Kyoto, Japan*

ARTICLE INFO

Keywords:
Gas hydrate
Chloride
Temperature
Fluid advection

ABSTRACT

We estimate the rate of upward pore fluid flow and chlorinity (Cl^-) concentrations at depth through a joint analysis of Cl^- concentration and temperature versus depth profiles obtained from gas hydrate related test sites drilled and cored in the Krishna-Godavari Basin off the eastern coast of India. Cl^-, measured on conventional core samples, decreases with depth at all sites but some of the Cl^-profiles show a prominent convex shape, whereas in situ temperature profiles, obtained by the Advanced Piston Coring Temperature probe, are mostly linear at all sites established during the National Gas Hydrate Program 02 Expedition (NGHP-02).

Assuming a one-dimensional, time-dependent model for the advection of pore fluid including the sedimentation effect and depth-dependent diffusivity, we estimate darcy velocity and the Cl^- concentrations at depth. The best-fit darcy velocity of $1.2–1.6 \times 10^{-11}$ m/s was estimated for the sites along the crest of the regional anticlinal structure in the NGHP-02 Area B, which was significantly faster than those on the flanks of the anticline. Because the thermal diffusion coefficient is much larger than the chloride ion diffusion coefficient, estimated darcy velocities are not great enough to generate nonlinear temperature profiles with depth, which is consistent with observed linear thermal profiles.

1. Introduction

In 2006, National Gas Hydrate Program Expedition 01 (NGHP-01) was led by the Indian Directorate General of Hydrocarbons (DGH) and with support from the U.S. Geological Survey (USGS), was carried out with *D/V JOIDES* Resolution off the coast of India, in order to contribute new data on the occurrence of gas hydrate systems and to advance understanding of the controls on the formation of gas hydrate accumulations in nature (Collet, 2014; NGHP Expedition 02 Scientists, 2015a). During the expedition, gas hydrate was discovered in numerous complex geologic settings. In 2015, a follow-up drilling expedition was carried out. The primary goal of National Gas Hydrate Program Expedition 02 (NGHP-02) was to conduct scientific ocean drilling/coring, logging, and analytical activities to assess the geologic occurrence, regional context, and characteristics of gas hydrate deposits along the eastern continental margin of India (Collett et al., 2019). The areas

---

[*] Corresponding author. Earthquake Research Institute, the University of Tokyo, Japan.
E-mail address: masa@eri.u-tokyo.ac.jp (M. Kinoshita).

https://doi.org/10.1016/j.marpetgeo.2018.12.049
Received 25 March 2018; Received in revised form 21 December 2018; Accepted 30 December 2018

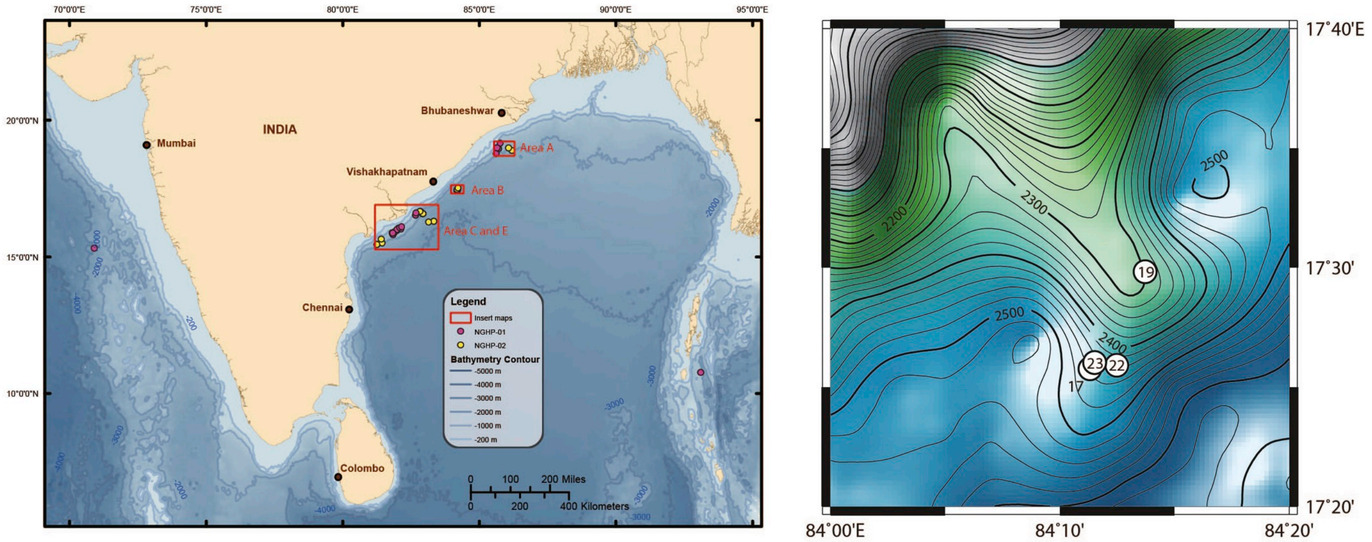

Fig. 1. (Left) Index map showing the location of NGHP-02 drill sites. (Right) Bathymetry in Area B. White circles are locations of drill sites, NGHP-02-17, −19, −22 and −23.

explored during NGHP-02 included scientific drill sites in the Krishna-Godavari and Mahanadi Basins off the eastern coast of India (Fig. 1: Areas A, B, C, and E).

A key question related to the hydrate abundance is how the methane is supplied to the hydrate stability zone. One of the sources is upward migrating pore fluids from deeper in the basin the carries deep-sourced methane gas into the overlying gas hydrate stability zone. Davie and Buffett (2001) introduced a numerical model to predict the volume and distribution of gas hydrate in deep continental margins where sedimentation adds organic material to the area of the gas hydrate stability zone. They also introduced the advective fluid input from below. If the fluid input from depth exists, it can be detected as non-linear anomalies in solutes that are carried with the pore fluid flow.

During the expedition, measurements of chlorinity and chloride ion concentrations (Cl—) within pore-waters recovered from sediment cores and in situ temperature surveys were conducted in most of the established core holes. Chloride ion concentrations (Cl^-) are one of the key geochemical parameters used to identify and characterize gas-hydrate-bearing sediments. Ijiri et al. (2019) analyze recovered pore-water samples, and suggested that the decrease of Cl^- is attributed to upward advection of low-Cl^- fluid derived from clay mineral dehydration, as suggested by Cl^- concentrations and $\delta^{18}O$ and δD values.

In this paper, we estimate the pore fluid vertical flux rate and Cl^- at depth as derived from conventional core samples through a joint analysis of Cl^- concentration and temperature depth profiles obtained from the gas hydrate research core sites established in the Krishna-Godavari Basin off the eastern coast of India. We focus on 4 core sites in Area B (Sites NGHP-02-17, −19, −22 and −23).

2. Geological setting

The main feature of Area-B (Fig. 1) is a large regional elongated anticlinal structure that is aligned perpendicular to the continental slope. The BSRs (Bottom Simulating Reflectors) were identified at depths nearly ~300 m below seafloor (mbsf) along the axis of the anticline. Sites NGHP-02-16, −17 and −23 were drilled through the crest of the anticline, whereas Sites NGHP-02-19 and −22 were drilled along the flank of the anticline. Two potential hydrate reservoir systems were identified in Area B, including an upper (R1) and a lower (R2) reservoir section. The upper reservoir facies are characterized by a relatively complex occurrence of both pore-filling and fracture-filling gas hydrates (Collett et al., 2019). The lower hydrate reservoir section (R2) as indicted by downhole LWD log at 270–290 mbsf and appears to extend across the entire anticlinal structure. The R2 reservoir section is characterized by high natural gamma radiation, high bulk density and lower porosity log values, and high electrical resistivity.

At Site NGHP-02-17, two hydrate reservoir sections are identified from LWD logs, R1 between 171.3 and 175.8 mbsf and R2 between 259.3 and 290.3 mbsf. The BSR is identified at ~320 mbsf below R2. A total of 50 cores were recovered including 9 pressure cores and 20 of the cores exhibited evidence of gas hydrate.

Site NGHP-02-23, located close to but slightly upslope of Site NGHP-02-17, was drilled through the crest of anticline. Two hydrate reservoir sections are identified from LWD logs, R1 between 181.3 and 188 mbsf and R2 between 259.3 and 290.3 mbsf. The BSR is identified at ~290 mbsf in the lower part of R2. A total of 48 cores including 11 pressure cores were taken.

Site NGHP-02-22 is located ~2 km to the east of Sites NGHP-02-17 and NGHP-02-17-23, in a flank region of the anticline. Two hydrate reservoir sections are identified from LWD logs, R1 between 207.7 and 234.8 mbsf and R2 between 368.6 and 386.5mbsf. The BSR is identified at ~285 mbsf, above the flank of anticline. A total of 49 cores including 9 pressure cores ware recovered.

Site NGHP-02-19 is in a flank position of the anticline in Area B. Unit II (mica-bearing silty clay) and is compared to that at Site NGHP-02-22. A hydrate reservoir section R1 is identified between 305.2 and 372 mbsf, from LWD resistivity logs. A total of 50 cores were recovered, including 6 pressure cores.

3. Methods of data acquisition

3.1. Cl^- concentration

Chloride (Cl^-) concentration in the pore water were measured on pore fluids squeezed from whole-round core samples (Ijiri et al., 2019). Sampling locations were carefully selected to avoid intervals with drilling disturbances, and intervals with mousse-like structures or sediments disturbed by hydrate dissociation were selected for sampling.

Concentrations of Cl^- and SO_4^{2-} in the pore water samples were analyzed on shipboard with an ion chromatograph (Dionex ICS-1500 ion chromatograph) with an anion column (Ijiri et al., 2019). Analytical precision was estimated to be within 1%, from repeated measurements of the same samples.

Ijiri et al. (2019) identified that sulfate (SO_4^{2-}) concentration from some interstitial fluid samples indicated contamination by drilling. Using sulfate concentration data, Ijiri et al. applied a correction of Cl^- concentration for the contamination by drilling fluid. We use these corrected Cl^- concentration values for our analysis.

3.2. Porosity and thermal conductivity

Porosities were measured onboard Chikyu for ~10 mL bulk volume samples taken from core samples (Kumar et al., 2019; Tanikawa et al., 2019; NGHP Expedition 02 Scientists, 2015c). Measurement interval depended on the lithology, but was typically at every 5 m. Porosity was calculated from wet and dry weight and dry (grain) volume (Blum, 1997).

Thermal conductivity values were measured onboard Chikyu for the whole-round core samples (Waite et al., 2019), by using a needle probe technique (Von Herzen and Maxwell, 1959). Measurement interval was around 5 m.

3.3. In situ temperature with APCT tool

During this expedition, in situ temperature measurements were carried out using the Advanced Piston Coring Temperature ver. 3 (APCT-3) tool (Heesemann et al., 2006), which is used with the hydraulic piston coring system (HPCS). Fig. 3 shows the temperature profiles with depth at sites in Area B. The formation temperature measurement was acquired with every third or fourth HPCS core (i.e. 30–40 m depth spacing). The sensor was calibrated for a working range of 0°–45 °C. Even when very high-quality data is collected, ambiguities in processing generally result in uncertainties in equilibrium temperatures not smaller than 0.1 °C–0.2 °C (Heesemann et al., 2006; Kinoshita et al., 2015).

4. Data

4.1. Cl^- concentration

Fig. 2 shows the Cl^- concentration profile vs. depth for a total of 4 sites cored during the expedition NGHP-02 in Area B. Circles are data from Hydraulic Piston Core System (HPCS), and dots are from Extended Shoe Coring System (ESCS) (Collett et al., 2019). Note that the data from pressure cores are not included here, because they were contaminated with the fresh water that was used for pressure core operations (Ijiri, 2019).

Cl^- concentration at the seafloor is ~560 mM at all sites, equivalent to the concentration of Cl^- in sea water. In Area B sites, Cl^- concentration exponentially decreases with increasing depth, with the most pronounced gradient in the shallower section within 150 mbsf as acquired by HPCS coring. Cl^- concentrations in deeper intervals, however, are more variable. Low Cl^- concentration spikes are likely caused by fresh water from dissociated hydrate upon core recovery (Ussler and Paull, 2001). Other more scattered data points mostly shifted toward high Cl^- concentrations are from samples cored with ESCS tool, which are likely caused by the drilling disturbance where the mud fluid (mostly seawater) was mixed with the in situ (low Cl^-) pore fluids during coring. We removed both negative spikes and data from ESCS cores, and used only data from HPCS cores for further analyses. Thus, the interpretations in this paper are based on data shallower than ~200 mbsf.

4.2. Porosity and thermal conductivity

Fig. 3 shows porosity and thermal conductivity vs. depth profiles measured onboard from 4 sites (Sites NGHP-02-17, −19, −22, and −23) in Area B (Fig. 1). The porosity values on the seafloor are ~80% for these sites, and decrease to ~65% at ~80 mbsf. Then they increase downward below 80 mbsf and reach maximum around 70% at ~250 mbsf, then decrease rapidly downward to ~50%. Through laboratory consolidation tests, this trend does not follow a typical compaction. Tanikawa et al. (2019) indicated that porosity is anomalously large at greater depths, which they interpret as a sign of overpressure.

4.3. In situ temperature

Temperatures basically increase linearly with increasing depth (Waite et al., 2019). A temperature profile can be non-linear either if seafloor temperature varies with time, if thermal conductivity varies with depth, or in a region of vertical advective fluid flow. We have no data on the time variation of seafloor temperature, but the deep-water depth (~2500 m) will probably preclude any significant temperature variation near the seafloor.

The heat flow is estimated as a gradient of in situ temperature versus thermal resistance that is calculated from thermal conductivities

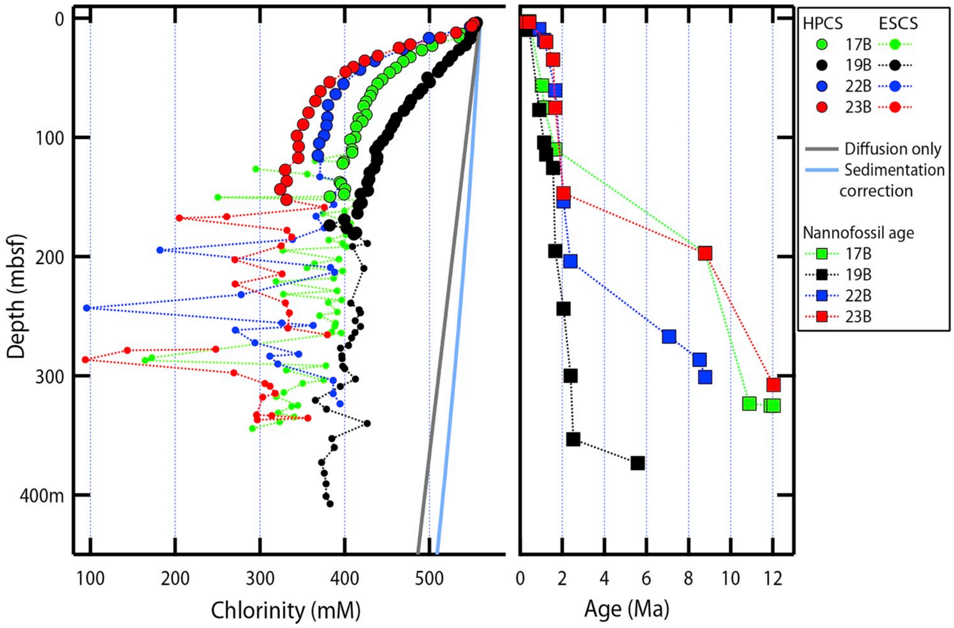

Fig. 2. (Left) Conventional core pore-water Cl^- concentration depth profiles for core samples acquired in Areas B. Larger symbols are from HPCS cores, and smaller symbols are from ESCS cores (not used in the analysis). Gray and blue lines are for diffusion only case and for sedimentation case, respectively, assuming a basal Cl^- value of 315 mM at 1500 mbsf. See Discussion section for sedimentation correction. (Right) Age-depth profiles determined from nannofossils. (For interpretation of the references to colour in this figure legend, the reader is referred to the Web version of this article.)

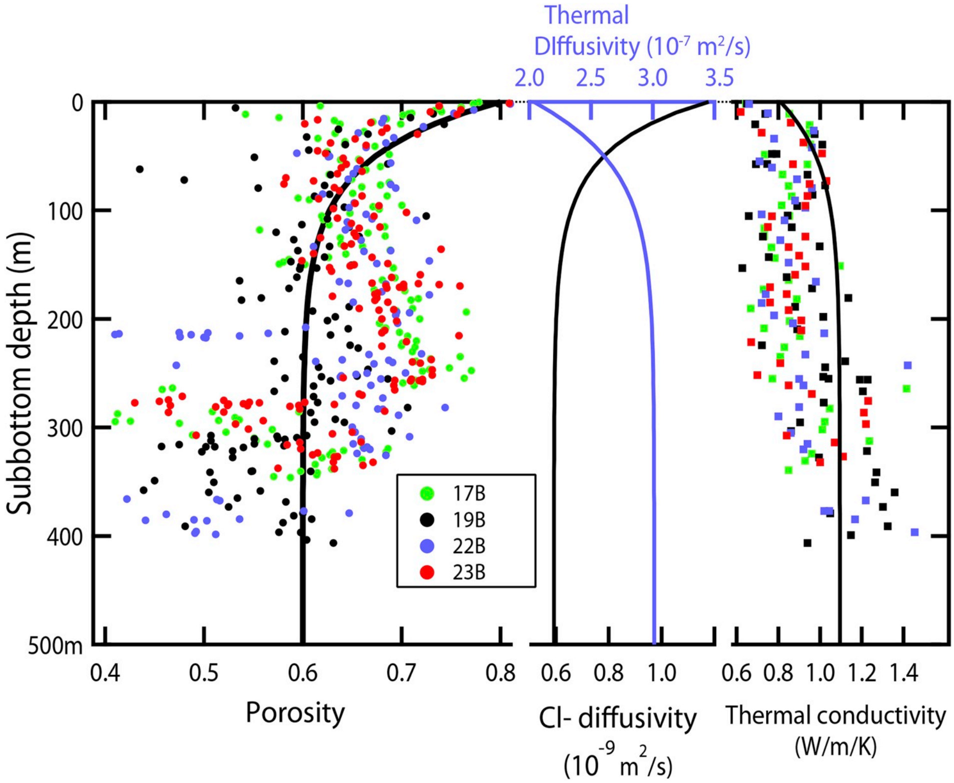

Fig. 3. Porosity (left) and thermal conductivity (right) versus depth data acquired at Sites NGHP-02-17, −19, −22, and −23, obtained from core samples. Solid curves are derived from empirical equation (see text for details). (Middle) Cl^- diffusivity derived from the porosity curve, and thermal diffusivity derived from thermal conductivity curve. These solid curves are used for numerical calculation.

(e.g., Bullard, 1954). In Area B, the heat flow value ranges from 55 to 58 mW/m^2.

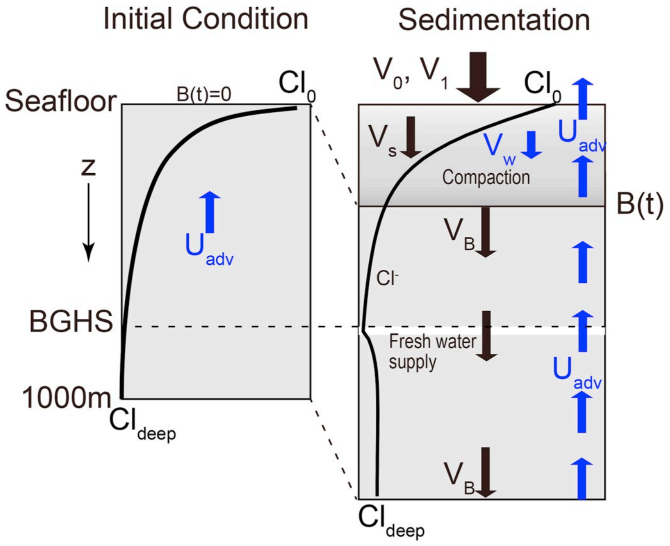

Fig. 4. Model configuration showing the sedimentation velocity, inflow from depth, and schematic plot of Cl^- profile. (Left) Initial condition of Cl^- concentration. C_0: Cl^- concentration on the seafloor, Cl_{deep}: Cl^- concentration at 1000 m below seafloor. BGHS = Base depth of Gas Hydrate Stability. (Right) Snapshot during the sedimentation process. *B(t)*: Depth to the base of sedimented strata; V_B: subsidence velocity of the base of sedimented strata; V_0, V_1: Sedimentation velocity (2 stages); V_s, V_w: Particle velocity of solid matrix and pore fluid due to sediment compaction. U_{adv}: darcy velocity of the inflow from below. Note that all the velocities are positive downward.

5. Numerical estimation of Cl^- and temperature profiles

5.1. Overview

The Cl^- concentration versus depth profiles in Area B decrease exponentially with increasing depth (Fig. 2). A steady-state, diffusive mixing model between seawater and deep-seated low-Cl^- water should produce a simple, almost linear Cl^- vs. depth profile. The observed concave-down profiles indicate an upward fluid advection with low-Cl^- water at depth.

The K-G Basin accumulates a large amount of sediments, leading to a high sedimentation rate even in the anticline in Area B. As deposited material is buried, the pore fluid is also buried. As the pressure (overburden) increases, the sediment will release its pore fluid due to compaction. This pore fluid will eventually escape to the seafloor. Fig. 4 schematically explain the sedimentation and fluid migration in the K-G Basin.

As they are buried deeper, the temperature increases due to the geothermal gradient, which will cause dissociation of methane hydrate when the buried sediment crosses the base of gas-hydrate stability (BGHS). This process produces fresh water, decreasing Cl^- concentration depending on the hydrate saturation. Then the pore fluids with less Cl^- ions diffuse upward and downward. In addition to such internally-generated fluids, there is the inflow of pore fluid from deeper strata, which add an advective contribution to the Cl^- profile. As the result of these processes, the Cl^- concentration should vary with depth and with time.

Sub-bottom temperatures (T) is also affected by sedimentation, compaction-driven fluid flow, inflow from depth, and thermal diffusion. The difference between Cl— and T is the magnitude of diffusivity.

First, we explain the methods to numerically calculate the time variation of chlorinity at 4 sites in Area B. We followed the method developed by Davie and Buffett (2001), based on the mass balance of sediment, pore fluid and the mass balance of dissolved methane and chloride ions. We considered continuous sedimentation on the seafloor, sediment compaction and dewatering (according to Hutchison (1985)), a constant-rate upward darcy flow of pore fluid, and the diffusion of Cl ions, and the effect of hydrate dissociation. For simplicity we did not simulate the change in hydrate saturation but kept it constant above

BGHS and zero below BGHS. This approach is the same as used in Toki et al. (2017) for the Nankai Trough forearc basin.

The goal is to estimate the most appropriate inflow of pore fluid (U_{adv}) and Cl$^-$ concentration at depth (Cl_{deep}) to best explain the Cl$^-$ profile at each site, i.e. to minimize the root-mean square (RMS) by means of a grid search approach.

5.2. Cl$^-$ modeling

5.2.1. Governing equation

The Cl$^-$ concentration is governed by the diffusion equation with advective term:

$$\varnothing(1 - S_h)\frac{\partial c_c}{\partial t} + U_w \cdot \frac{\partial c_c}{\partial z} = \frac{\partial}{\partial z}\left[D_c \varnothing(1 - S_h)\frac{\partial c_c}{\partial z}\right], \qquad (1)$$

where *Cc* the Cl$^-$ concentration, ϕ the porosity, *Sh* the hydrate saturation, U_w the total volumetric fluid flux per unit area ($= \phi$ (1-*Sh*) $V_w + U_{adv}$), D_c the diffusion coefficient of Cl ions. These parameters are defined in the following subsections. By numerical integration we calculate the time and depth variation of Cc.

5.2.2. Sedimentation effect

When the sedimentation rate is higher than the diffusion rate of Cl$^-$ concentration, Cl$^-$ vs. depth profile is temporarily affected by sedimentation and differs from a steady state. During the NGHP-02 expedition, nannofossil age data were obtained (NGHP Expedition 02 scientists, 2015b). Table 1 shows a summary of sedimentation at each site in Area B. For instance, at Site NGHP-02-23, 135 m of sediments deposited between 2.4 Ma and 1.56 Ma (stage 1), followed by 35 m deposition after 1.56 Ma to present (stage 2). Prior to stage 1, we ignore the sedimentation effect because it is very slow at all sites (Fig. 2). As such, we define the seafloor before stage 1 sedimentation starts “the sediment/basement interface”.

The sedimentation rate is estimated from the sediment age-depth relationship reported in earlier studies (Collett et al., 2019). The depositional thickness of sediments at each depth horizon has been corrected to account for the vertical decrease in thickness due to the overburden pressure (Hutchison, 1985).

We set the z-coordinate and velocity values positive downward in which z = 0 on the seafloor. The burial of sediments as sedimentation continues is expressed by the downward movement of the sediment/basement interface relative to the seafloor.

The volumetric transport rate of solid matrix per unit area (U_s) and the volumetric fluid flow velocity per unit area due to compaction (U_{com}) does not depend on the depth, considering the mass conservation in one dimension (but varies with time). The pore fluid flow is also affected by the advection from a deeper portion (U_{adv}). We assume a constant value for U_{adv}. The total volumetric flux per unit area of the pore fluid (U_w) can be expressed as:

$$U_w = U_{com} + U_{adv}. \qquad (2)$$

According to Hutchison (1985), U_{com} and U_s are expressed as:

$$U_{com} = V_w \phi = V_0(1 - \phi_0)\frac{\phi(B(t))}{1 - \phi(B(t))} \qquad (3)$$

$$U_s = V_s(1 - \phi) = V_0(1 - \phi_0), \qquad (4)$$

where V_0 and V_1 are the sedimentation velocities, V_s, V_w the particle velocity of solid matrix and pore fluid, respectively, and B(t) the depth to the sediment/basement interface. The values of V_s, V_w and B(t) are calculated according to Hutchison (1985).

5.2.3. Porosity based on normal compaction assumption

Porosity data were obtained on core samples (Fig. 3; Collett et al., 2019). Tanikawa et al. (2019) estimated an overpressure, based on the high porosity anomaly combined with their consolidation tests. Such overpressure may introduce a time-dependent fluid expulsion depending on the permeability, and thus the porosity curve may change in the geological time scale.

Since we have no information on its temporal change, we assume here a normal consolidation state, i.e. the porosity does not vary with time. Then we used the Modified Athy's law, where the porosity exponentially approaches to a certain value:

$$\phi(z) = \phi_\infty + (\phi_0 - \phi_\infty)\exp\left(-\frac{z}{\lambda}\right), \qquad (5)$$

where ϕ the porosity, ϕ_∞ the porosity at depth. ϕ_0 the porosity just below the seafloor, and λ a constant. Based on the porosity measured on core samples, we set $\phi_\infty = 0.6$, $\phi_0 = 0.8$, and $\lambda = 50$ [m].

5.2.4. Diffusivity of Cl−

Li and Sandra (1974) compiled the diffusivities of ions in sediments with respect to temperature, pressure, and tortuosity. Based on the compilation of existing data and laboratory experiments, Van Loon and Mibus (2015) proposed an empirical relationship between accessible porosity and the effective diffusion coefficient of Cl$^-$. They modified the Archie's law between electrical resistivity and porosity. In this paper we used relationship by Van Loon and Mibus (2015):

$$D_e = D_W \cdot \phi^{m_1} + B \cdot \phi^{m_2}, \qquad (6)$$

where D_e the effective diffusion coefficient of Cl$^-$, D_w the diffusion coefficient in water, ϕ the diffusion-accessible porosity, m_1, m_2 and B the constants. Here we use $D_w = 2*10^{-9}$ [m^2/s], $m_1 = 2.4$, $m_2 = 1$, and $B = 10^{-11}$.

5.2.5. Hydrate saturation

Analysis by Davie and Buffett (2001) includes the formation and dissociation process of methane hydrate. For simplicity, we do not simulate the change in hydrate saturation (S_h), but S_h is set to be a

Table 1
Parameters for sedimentation (modified from Collett et al., 2019).

Site	Parameters used for calculation								Results		
	Sedimentaion Stage 1			Sedimentaion Stage 2			Depth to BSR	Hydrate saturation	Cl− at depth	Fluid influx from depth	
	Age range	Thickness	Rate	Age range	Thickness	Rate	mbsf	Sh	Cldeep	Uadv	Uadv
	MyBP	m	m/ky	MyBP	m	m/ky		%	mM	$*10^{-12}$ m/s	mm/yr
19	2.4–0.44	~340	0.32	0.44 – Present	~10	0.03	320	0	370 ± 40	6 ± 1	0.2
17	2.1–0.44	~150	0.15	0.44 – Present	~5	0.02	290	10	400 ± 20	15 ± 5	0.47
22	2.39–1.14	~185	0.26	1.14 – Present	~20	0.02	290	10	370 ± 40	16 ± 7	0.5
23	2.4–1.56	~135	0.27	1.56 – Present	~35	0.03	290	30	320 ± 20	12 ± 3	0.38

Note: Site: NGHP-02-##. Age: depositional age. Thickness: Sediment thickness on core samples. Rate: Sediment accumulation rate (depositional particle velocity on the seafloor). Note that the ‘Rate’ does not match the ‘Thick’/‘Age interval’, because of the compaction of sediments.

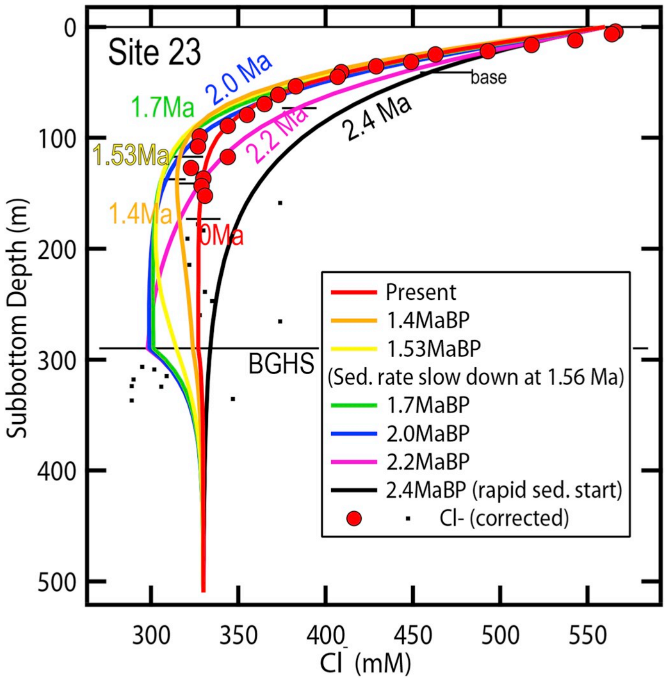

Fig. 5. Time variation of Cl^- vs. depth profiles at Site NGHP-02-23. A black curve labeled "2.4 Ma" is an initial condition. Note that Cl^- concentration at the seafloor (0 m) and at 1000 m below seafloor are fixed at 560 mM and Cl_{deep} throughout the simulation. Horizontal bars labeled "base" are the depth at the base of sedimentation. "BSR" is the depth of Bottom Simulating Reflector. Colored circles are Cl^- concentration data from HPCS cores, which were used for the fitting; black dots are ones from ESCS/HPCS cores that not used for the fitting. For this example, sedimentation rate (corrected for a compaction) was faster between 2.4 Ma and 1.56 Ma.

constant above the BGHS and to zero underneath the BGHS. We set S_h at each site according to Collett et al. (2019) (1–30%; Table 1). As sediments are buried, methane hydrates dissociate as they cross BGHS, generating Cl-depleted fluid. We included this effect in the analysis. However, we did not include the increase in Cl^- concentration due to hydrate formation, because we do not know how and where it occurs. As such, estimated Cl^- concentration may be biased to a lower value.

5.2.6. Boundary and initial conditions

Selection of the depth of bottom boundary needed some consideration. Observed Cl^- vs. depth profiles (Fig. 2) exponentially decrease and converge to certain values at depths greater than ~300 m. Since the temperature is too low to drive in situ dehydration of clay minerals at shallow depths, the observed low Cl^- fluid should be transported from below. Reduction of Cl^- at depth is primarily caused by the dehydration of clay minerals. Such dehydration occurs at the temperature range of 60–150 °C (e.g. Saffer and Tobin, 2011), or at the depth range of 1000–2700 m as inferred from APCT temperature profile in Area B. Here we tested the bottom boundary depth at 1000 m and 2000m, both of which provided identical results. Thus we use 1000 m as the depth of the bottom boundary. The Cl^- concentration is set at 560 mM on the seafloor and Cl_{deep} at 1000 m below seafloor.

We start calculation after the stage 1 (Table 1). The initial Cl^- concentration profile is defined as a diffusional equilibrium between seafloor (560 mM) and 1000 m below seafloor (Cl_{deep}), with advective fluid flow (Table 1 and Fig. 4). Advective fluid flow (U_{adv}) is kept constant independent of the depth and throughout the simulation. Sedimentation rates are defined in Table 1.

5.3. Geothermal modeling

5.3.1. Governing equation

The equation to estimate the thermal regime under a 1-D diffusion with pore fluid advection is basically the same as the case of Cl^- diffusion. It is different, however, in that the thermal diffusion takes place in both the solid grain and the pore fluid, whereas the advective heat transport occurs only within the pore space. According to Hutchison (1985), the governing equation is:

$$(\rho_w c_w \phi + \rho_s c_s (1-\phi))\frac{\partial T}{\partial t} + (U_w + U_s)\cdot\frac{\partial T}{\partial z} = \frac{\partial}{\partial z}\left[K\frac{\partial T}{\partial z}\right], \qquad (7)$$

Where ρ_w, c_w are the density and specific heat of water, ρ_s, c_s are those of solid matrix, U_w and U_s the total volumetric flux of pore fluid and solid matrix per unit area (eqs. (2)–(4)), and K the thermal conductivity.

5.3.2. Thermal conductivity

In general, thermal conductivity vs. depth profiles at Sites NGHP-02-17, −19, −22 and −23 in Area B follow the similar trend to each other, so we created a single conductivity profile using the porosity curve (eq. (5)) as:

$$\mathrm{K} = K_w^{\phi} K_s^{1-\phi}, \qquad (8)$$

where K_w and K_s are the thermal conductivity of water and solid matrix, respectively. This model (e.g. Brigaud and Vasseur, 1989) is widely used for marine sediments.

Thermal diffusivity (κ) is derived from thermal conductivity and porosity as $\kappa = \mathrm{K}/(\rho_w c_w \phi + \rho_s c_s (1-\phi))$ (Fig. 3). Thermal diffusivity ($2–3 \times 10^{-7}\ m^2/s$) is larger than Cl^- diffusivity by more than 200 times. The thermal diffusivity is reported as $> 2 \times 10^{-7}\ m^2/s$ for marine sediments (e.g. Goto and Matsubayashi, 2008; Goto and Matsubayashi, 2009), or $3.1–3.3 \times 10^{-7}\ m^2/s$ (Kumar et al., 2004) for hydrate-bearing sediments. Our estimate is consistent with these values. Thus, any geothermal transients caused by sedimentation or fluid migration should decay faster than Cl^- transients.

5.4. Results of simulation

5.4.1. Cl^- concentration

Fig. 5 shows the time variation of Cl^- vs. depth profiles at Site NGHP-02-23. A black curve labeled "2.4 Ma" is an initial condition (linear profile). Note that Cl^- concentration at the seafloor (0 m) and at 1000 m below seafloor are fixed at 560 mM and Cl_{deep} throughout the simulation. Horizontal bars labeled "base" is the depth at the base of sedimentation. "BSR" is the depth of Bottom Simulating Reflector. Colored circles are Cl^- concentration data from HPCS cores, which were used for the fitting; black dots are ones from ESCS/HPCS cores that were not used for the fitting. For this example, sedimentation rate (corrected for a compaction) was faster between 2.4 Ma and 1.56 Ma. During that period negative excursions are clear at BSR. It is caused by the hydrate dissociation in the pore fluid due to temperature increase there, and the asymmetric shape (gentle convex shape above BSR and steep curve below) is due to the upward flow from deeper portion (U_{adv}). This upward flow (U_{adv}) is greater than the downward flow due to compaction (U_{com}), giving rise to the net upward flow generating convex Cl^- profiles. By the end of rapid sedimentation period, Cl^- profile is almost fitting to the observation. After 1.56 Ma, sedimentation rate decreased by one order of magnitude. It also reduces the rate of dissociation, and data kink at BSR diminishes due to diffusion.

Fig. 6(a) shows both the observed Cl^- data (circles) and calculated Cl^- profiles at present (red curves) at Sites NGHP-02-19, −17, −22 and −23 in Area B. Numbers attached to the red curves indicate the upward darcy flow rate, U_{adv} ($x10^{-12}$ m/s). Red dashed curves are the present Cl^- profiles with $U_{adv} = 0$, a case with sedimentation/compaction and diffusion only.

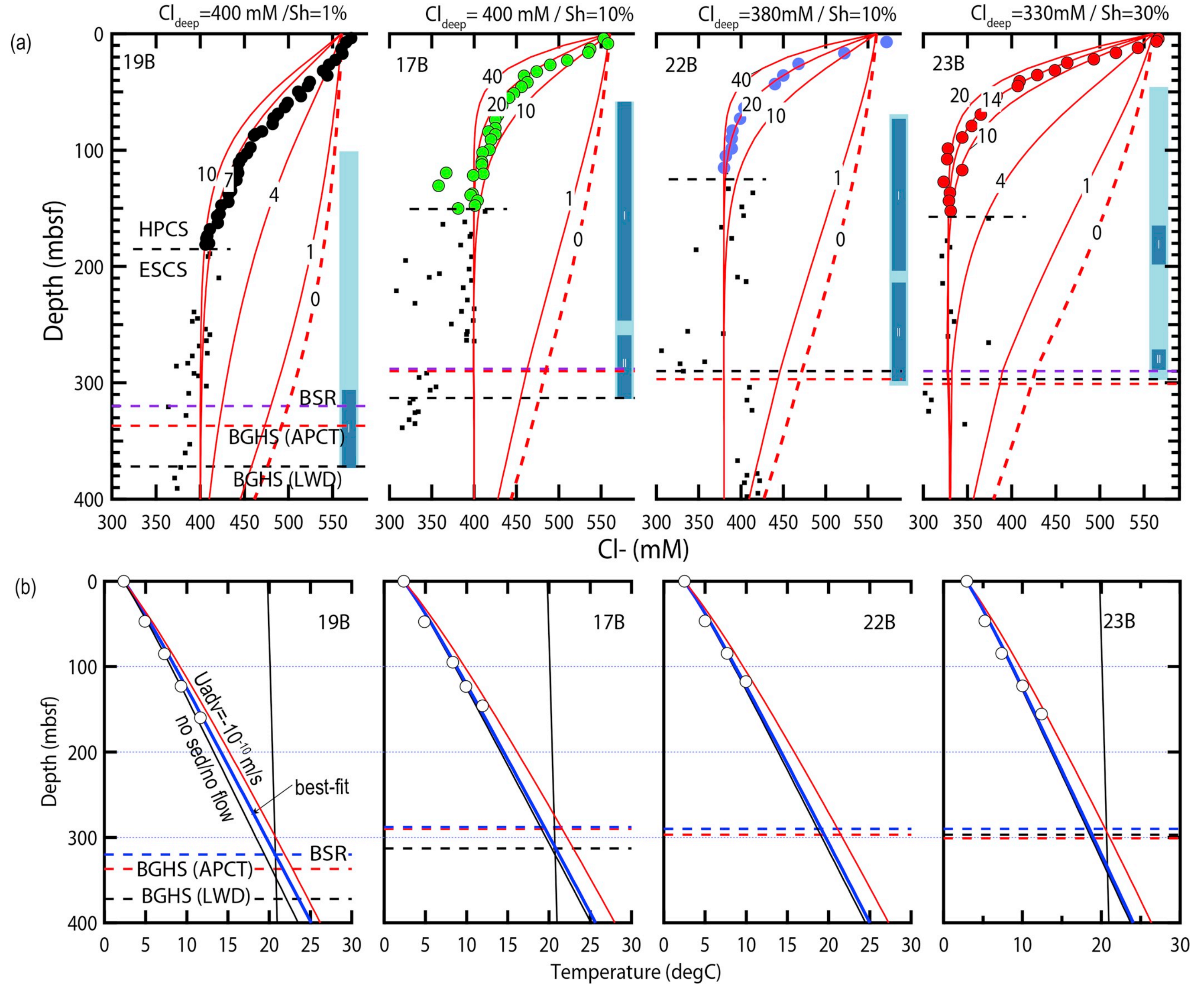

Fig. 6. (a) Cl^- concentration vs. depth profiles for Sites NGHP-02-19, −17, −22, −23 in Area B. Larger circles are from HPCS cores, and dots are from ESCS cores. Numbers attached to the red curves indicate the upward darcy flow rate, U_{adv} ($*10^{-12}$ m/s). Red dashed curves are the present Cl^- profiles with $U_{adv} = 0$, a case with sedimentation/compaction and diffusion only. In the column to the right of each site, dark blue zones indicate areas of concentrated gas hydrate. (b)Temperature vs. depth profiles for sites in Area B. Circles are the measured in situ temperatures. Curves are the results of numerical calculation. Thin black, thick blue, and thin red curves correspond to the reference (no sedimentation, no inflow), the best-fit U_{adv}, and U_{adv} = -1x10^{-10} m/s cases, respectively. BSR: Depth of the Bottom Simulating Reflector. The depth to the base of gas hydrate stability (BGHS (APCT)) is estimated from these predicted temperatures. (For interpretation of the references to colour in this figure legend, the reader is referred to the Web version of this article.)

To find the best-fit profile at each site, we calculated the root-mean square (RMS) values of misfit between calculated and observed Cl^- concentration for a range of Cl_{deep} and U_{adv}. Fig. 7 shows the RMS distribution at 4 sites, where the vertical axes are U_{adv} and the horizontal axes are Cl_{deep}. Color images are the RMS values, in which blue region correspond to RMS minimum, and the stars correspond to the 'best-fit' cases. For comparison, these 'blue' region and a star at each site are also shown on the lower-left panel (19B). The best-fit values of Cl_{deep} and U_{adv} are listed in Table 1.

We see that U_{adv} is more sensitive than Cl_{deep} to the variation in RMS, suggesting that the observed Cl^- data can better constrain U_{adv} than Cl_{deep}. Table 1 is a list of best-fit results with uncertainties, which are based on the 'blue' area in Fig. 7. At Site NGHP-02-19, U_{adv} is estimated as $6 \pm 1 \times 10^{-12}$ m/s, while it is 15 ± 5, 16 ± 7, 12 ± 3 m/s at Sites NGHP-02-17, −22 and −23, respectively. The latter 3 values are consistent with each other, and are significantly higher than at Site NGHP-02-19. All 4 sites are located near the ridge of anticlines (Fig. 1), the latter 3 sites are located within 1 km to each other, and Site NGHP-02-19 is 7.5–9 km to the NNE of them.

The best-fit Cl^- concentration at the bottom (Cl_{deep}) ranges 300–420 mM. However, their uncertainties are large and overlap to each other, except it is low at Site NGHP-02-23 (320 mM).

5.4.2. Temperature profiles

As a reference, we tested a steady-state case without sedimentation and pore fluid flow (Fig. 6). Then some cases under the actual sedimentation rate are tested, where we set the inflow rate (U_{adv}) either to zero, to the best-fit value for Cl^- concentration profile (1 to -4x10^{-11} m/s), or to -1x10^{-10} m/s as an extreme case. Except for the extreme case with U_{adv} = -1x10^{-10} m/s, calculated temperature profiles are almost identical to each other. This is due to a large thermal diffusivity value larger than Cl^- diffusivity by more than two orders of magnitude. In other words, both the nonlinear Cl^- concentration and (almost) linear temperature profiles are the result of an upward pore

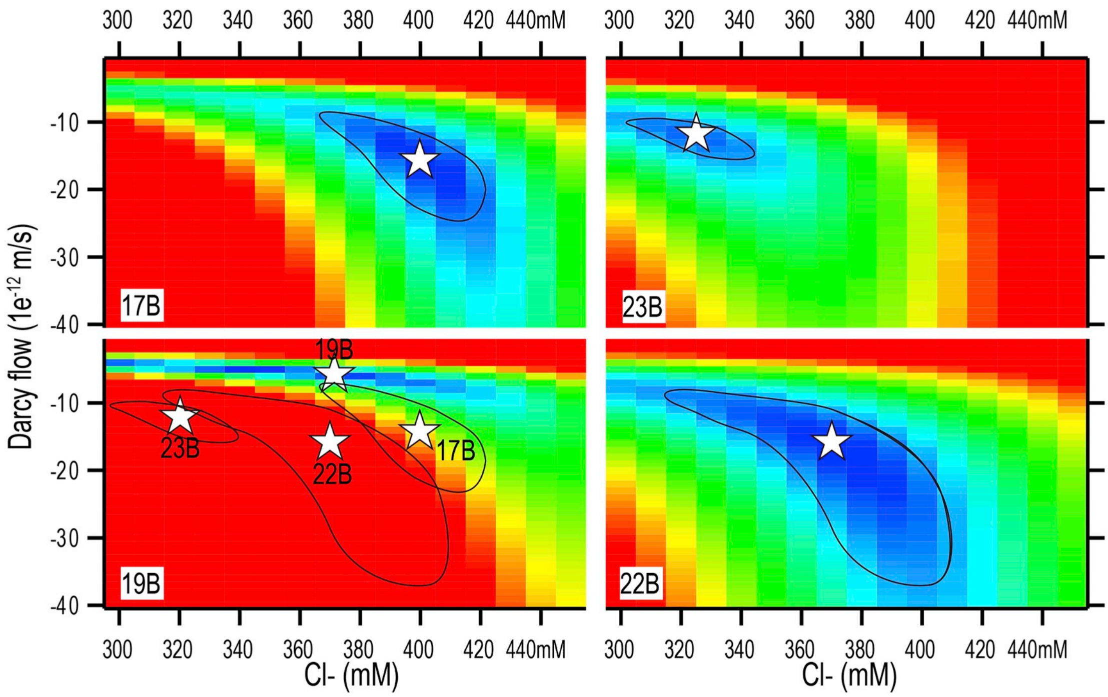

Fig. 7. RMS (root-mean square) distribution at 4 sites, where the vertical axes are U_{adv} and the horizontal axes are Cl_{deep}. Color images are the RMS values, in which blue region correspond to RMS minimum, and the stars correspond to the 'best-fit' cases. For comparison, these 'blue' region and a star at each site are also shown on the lower-left panel (Site NGHP-02-19B). The best-fit values of Cl_{deep} and U_{adv} are listed in Table 1. (For interpretation of the references to colour in this figure legend, the reader is referred to the Web version of this article.)

fluid flux.

6. Discussion

6.1. Other possible causes for nonlinear Cl^- profile

We analyzed the Cl^- and temperature profiles at 4 sites in Area B in the K-G Basin by considering the effects of sedimentation (i.e. burial and compaction-driven dewatering), advective fluid flow from depth, and hydrate dissociation. To explain both the Cl^- and temperature profiles, we found that a certain amount of advective upward flow of pore fluid is necessary at 4 sites in Area B. We discuss here whether there are any other factors that can contribute to make nonlinear Cl^- profile (but keep the linear temperature profile).

6.1.1. Dissociation of hydrate with higher saturation

We assumed a constant hydrate saturation (1% at Site NGHP-02-19, 10% at Sites NGHP-02–17 and −22, 30% at Site NGHP-02-23). If the hydrate saturation is higher, the more fresh water will be produced by hydrate dissociation as it is buried due to sedimentation. It leads to reduction of Cl^- concentration, thus the observed low Cl^- profile may be explained under a slower U_{adv} value than estimated here.

However, the age-depth curve in Fig. 2 tell us that the sedimentation rate decreased recently up to present at all sites. Under a slower sedimentation rate, the hydrate dissociation rate (thus the production rate of fresh water) also slows down. As shown in simulated Cl^- profiles (Fig. 6), the effect of low Cl^- is almost diminished at present. We believe that the higher hydrate saturation cannot be the primary source of observed nonlinear Cl^- profile.

6.1.2. Porosity anomaly

As noted in Sections 3.2 and 5.2, the measured porosity profile does not follow a typical compaction curve and increases between ~150 and 250 mbsf. We tested a model with this porosity trend at Site NGHP-02-23:

$$\phi(z) = 0.8 + (0.64 - 0.8)/50 * z \qquad (z = 0 \sim 50\text{ m})$$
$$\phi(z) = 0.64 + (0.68 - 0.64)/(250 - 50) * (z - 50) \qquad (z = 50 \sim 250\text{ m}),$$
$$\phi(z) = 0.68 + (0.6 - 0.68)/(300 - 250) * (z - 250) \qquad (z = 250 \sim 300\text{ m}).$$
$$\phi(z) = 0.6 \qquad (z > 300\text{ m}).$$

The result was compared with the normal compaction case, and their difference in Cl^- profile is less than 5 mM for each time step, and is negligible (less than 1 mM difference) at present.

6.2. Implication

Among 4 sites, Sites NGHP-02-17, −22, −23 which are close to each other would have a larger fluid input from deeper formation (U_{adv} = 12–16 * 10^{-11} m/s) than Site 19 (6*10^{-11} m/s). We believe that the large fluid input is a primary cause for hydrate-bearing sediments, as suggested by Ijiri et al. (2019).

Tanikawa et al. (2019) suggest the existence of overpressure zone at Sites NGHP-02-22 and −23 at a greater depth (> ~150 mbsf) where the porosity was enhanced. Tanikawa et al. (2019) also demonstrated that such an overpressure can be achieved if the influx from depth exceeds 10^{-11} m/s. Our estimation of U_{adv} at these sites, based on the shallow data from HPCS cores, are consistent with it. .

At these sites, fluid may be stored in high-porosity zones (150–250 m) and upward darcy flow may occur only above ~100 mbsf to the seafloor. In our 1-D model, this situation can be simulated as a low-Cl^- reservoir emplaced deeper than 150 m and a constant upward flow above it. Although our model assumes deeper low-Cl^- reservoir (> 1000 m), shallower reservoir model can reasonably explain the data to some extent. If the flow is intermittent or transient (but only above the reservoir), the concave-down profile varies with time; during the no-flow period the profile approaches to linear, whereas during the active flow period the profile becomes more concave.

However, our 1-D model is too simple to discuss more details about the depth and temporal variation of flow. It requires (at least) 3-D poroelastic modeling, which is beyond the scope of this paper.

7. Conclusions

We estimate here the upward pore fluid flux and Cl^- concentrations at depth (< 1000 mbsf) through a joint analysis of Cl^- and temperature depth profiles obtained in hydrate-bearing sediments associated with the NGHP-02 Area B in the Krishna-Godavari Basin off the eastern coast of India.

Cl^- concentrations in the pore fluid squeezed from conventional core samples decrease with depth at all sites cored in Area B. They show prominent convex shape, indicating upward pore fluid migration.

The volume flow rate and the Cl^- at depth are estimated at each site using the 1-D time-dependent model. The best-fit velocity is $1.2–1.6 \times 10^{-11}$ m/s at sites along the crest of the anticline (Sites NGHP-02-17, −22 and −23 in Area B), significantly faster than in flank (Site NGHP-02-19; $\sim 0.6 \times 10^{-11}$ m/s).

In situ temperature profiles are mostly linear with depth at all sites in Area B. The apparent disagreement with the nonlinear Cl^- profiles can be explained by the fact that ion (Cl^-) diffusivity is much lower than thermal diffusivity.

Acknowledgments

We thank the Ministry of Petroleum & Natural Gas in the Government of India, Oil and Natural Gas Corporation Ltd., Directorate General of Hydrocarbons, Oil India Ltd., GAIL (India) Ltd., Indian Oil Corporation Ltd., and all other NGHP partner organizations for providing us with the opportunity to contribute to the NGHP-02 Expedition and this special issue of the Journal of Marine and Petroleum Geology. We also appreciate all the technical and science support from Japan Agency for Marine-Earth Science and Technology, United States Geological Survey, U.S. Department of Energy, the National Institute of Advanced Industrial Science and Technology, Geotek Coring, and Schlumberger. We acknowledge the great support of technicians on D/V Chikyu. Excellent technical and logistical support on the drilling vessel D/V Chikyu was crucial for this research, which was funded by a special JAMSTEC grant for NGHP-02 related studies.

References

Blum, P., 1997. Physical properties handbook: a guide to the shipboard measurement of physical properties of deep-sea cores 26 ODP Tech. Notehttps://doi.org/10.2973/odp.tn.26.1997.

Brigaud, F., Vasseur, G., 1989. Mineralogy, porosity and fluid control on thermal conductivity of sedimentary rocks. Geophys. J. 98, 525–542.

Bullard, E.C., 1954. The flow of heat through the floor of the Atlantic Ocean. Proc. Roy. Soc. Lond. A 222, 408–429.

Collet, T., 2014. Preface: geologic implications of gas hydrates in the offshore of India: results of the national gas hydrate Program expedition 01. J. Marine Petrol. Geol. 58, 1–2. https://doi.org/10.1016/j.marpetgeo.2014.07.020.

Collett, T.S., Boswell, R., Waite, W.F., Kumar, P., Roy, S.K., Chopra, K., Singh, S.K., Yamada, Y., Tenma, N., Pohlman, J., Zyrianova, M., NGHP Expedition 02 Scientific Party, 2019. India National Gas Hydrate Program Expedition 02 summary of scientific results: gas hydrate systems along the eastern continental margin of India. J. Mar. Petrol. Geol. 108, 39–142.

Davie, M.K., Buffett, B.A., 2001. A numerical model for the formation of gas hydrate below the seafloor. J. Geophys. Res. 106, 497–514.

Goto, S., Matsubayashi, O., 2009. Relations between the thermal properties and porosity of sediments in the eastern flank of the Juan de Fuca Ridge. Earth Planets Space 61, 863–870.

Goto, S., Matsubayashi, O., 2008. Inversion of needle-probe data for sediment thermal properties of the eastern flank of the Juan de Fuca Ridge. J. Geophys. Res. 113, B08105. https://doi.org/10.1029/2007JB005119.

Heesemann, M., Villinger, H., Fisher, A.T., Tréhu, A.M., White, S., 2006. Data report: testing and deployment of the new APCT-3 tool to determine in situ temperatures while piston coring. In: In: Riedel, M., Collett, T.S., Malone, M.J., the Expedition 311 Scientists (Eds.), Proc IODP, vol. 311 Integrated Ocean Drilling Program Management International, Inc, Washington, DC. https://doi.org/10.2204/iodp.proc.311.108.2006.

Hutchison, I., 1985. The effects of sedimentation and compaction on oceanic heat flow. Geophys. J. Roy. Astron. Soc. 82, 439–459.

Ijiri, A., Haraguchi, S., Jiménez-Espejo, F.J., Komai, N., Suga, H., Kinoshita, M., Inagaki, F., Yamada, Y., NGHP Expedition 02 JAMSTEC Science Team, 2019. Origin of low-chloride fluid in sediments from 1 the eastern continental margin of India, results from the National Gas Hydrate Program Expedition 02. J. Mar. Petrol. Geol. 108, 377–388.

Kinoshita, M., Fukase, H., Goto, S., Toki, T., 2015. In situ thermal excursions detected in Nankai Trough forearc slope sediment at IODP NanTroSEIZE Site C0008. Earth Planets Space 67, 16. https://doi.org/10.1186/s40623-014-0171-1.

Kumar, P., Turner, D., Sloan, E.D., 2004. Thermal diffusivity measurements of porous methane hydrate and hydrate sediment mixtures. J. Geophys. Res. 109, B01207. https://doi.org/10.1029/2003JB002763.

Kumar, P., Collett, T.S., et al., 2019. India National Gas Hydrate Program Expedition-02: operational and technical summary. J. Mar. Petrol. Geol. 108, 3–38.

Li, Y.-H., Sandra, G., 1974. Diffusion of ions in sea-water and in deep-sea sediments. Geochem. Cosmochim. Acta 38, 703–714. https://doi.org/10.1016/0016-7037(74)90145-8.

NGHP Expedition 02 Scientists, 2015a. NGHP Expedition 02 summary. In: JAMSTEC Science Team, National Gas Hydrate Program R&D Expedition 02 Final Report. International Ocean Discovery Program, College Station, TX.

NGHP Expedition 02 Scientists, 2015b. Sediment age. In: JAMSTEC Science Team, National Gas Hydrate Program R&D Expedition 02 Final Report. International Ocean Discovery Program, College Station, TX.

NGHP Expedition 02 Scientists, 2015c. Laboratory methods. In: JAMSTEC Science Team, National Gas Hydrate Program R&D Expedition 02 Final Report. International Ocean Discovery Program, College Station, TX.

Saffer, D., Tobin, H., 2011. Hydrogeology and mechanics of subduction zone forearcs: fluid flow and pore pressure. Annu. Rev. Earth Planet Sci. 39, 157–186. https://doi.org/10.1146/annurev-earth-040610-133408. 2011.

Tanikawa, et al., 2019. Porosity, permeability, and grain size of sediment cores from gas-hydratebearing sites and their implication for overpressure in shallow argillaceous formations: Results from the national gas hydrate program expedition 02, Krishna-Godavari Basin, India. J. Mar. Petrol. Geol. 108, 332–347.

Toki, T., Kinoshita, M., Morita, S., Masuda, H., Rashid, H., Yoshinishi, H., Nakano, T., Noguchi, T., 2017. The vertical chloride ion profile at the IODP Site C0002, Kumano Basin, off coast of Japan. Tectonophysics. https://doi.org/10.1016/j.tecto.2016.11.029.

Ussler, W., Paull, C.K., 2001. Ion exclusion associated with marine gas hydrate deposits. In: Paull, C.K., Dillon, W.P. (Eds.), Natural Gas Hydrates: Occurrence, Distribution, and Detection. American Geophysical Union, Washington, D. C. https://doi.org/10.1029/GM124p0041.

Van Loon, L.R., Mibus, J., 2015. A Modified Version of Archie's Law to Estimate Effective Diffusion Coefficients of Radionuclides in Argillaceous Rocks and its Application in Safety Analysis Studies. https://doi.org/10.1016/j.apgeochem.2015.04.002.

Von Herzen, R.P., Maxwell, A.E., 1959. The measurement of thermal conductivity of deep-sea sediments by a needle-probe method. J. Geophys. Res. 64, 1557.

Waite, W.F., Ruppel, C., Collett, T.S., Schultheiss, P., Holland, M., Shukla, K.M., Kumar, P., 2019. Multi-measurement approach for establishing the base of gas hydrate occurrence in the Krishna-Godavari Basin for sites cored during Expedition NGHP-02 in the offshore of India. J. Mar. Petrol. Geol. 108, 296–320.